

Distance to healthy cardiovascular dynamics from fetal heart rate scale-dependent features in pregnant sheep model of human labor predicts cardiovascular decompensation

S.G. Roux ¹, N.B. Garnier ^{1,*}, P. Abry ¹, N. Gold ² and M.G. Frasch ³

¹ Laboratoire de Physique, Univ Lyon, Ens de Lyon, Univ Claude Bernard, CNRS, F-69342 Lyon, France;

²Department of Mathematics and Statistics, York University, Canada; Centre for Quantitative Analysis and Modelling, Fields Institute, Toronto, USA.

³ Dept. of OBGYN and the Center on Human Development and Disability, University of Washington, Seattle, USA

Abstract

The overarching goal of the present work is to contribute to the understanding of the relations between fetal heart rate (FHR) temporal dynamics and the well-being of the fetus, notably in terms of predicting cardiovascular decompensation (CVD). It makes uses of an established animal model of human labor, where fourteen near-term ovine fetuses subjected to umbilical cord occlusions (UCO) were instrumented to permit regular intermittent measurements of metabolites, pH, and continuous recording of electrocardiogram (ECG) and systemic arterial blood pressure (to identify CVD) during UCO. ECG-derived FHR was digitized at the sampling rate of 1000 Hz and resampled to 4Hz, as used in clinical routine. We focused on four FHR variability features which are tunable to temporal scales of FHR dynamics, robustly computable from FHR sampled at 4Hz and within short-time sliding windows, hence permitting a time-dependent, or local, analysis of FHR which helps dealing with signal noise. Results show the sensitivity of the proposed features for early detection of CVD, correlation to metabolites and pH, useful for early acidosis detection and the importance of coarse time scales (2.5 to 8 seconds) which are not disturbed by the low FHR sampling rate. Further, we introduce the performance of an individualized self-referencing metric of the distance to healthy state, based on a combination of the four features. We demonstrate that this novel metric, applied to clinically available FHR temporal dynamics alone, accurately predicts the time occurrence of CVD which heralds a clinically significant degradation of the fetal health reserve to tolerate the trial of labor.

Keywords: fetal heart rate, animal model of human labor, cardiovascular decompensation, distance to healthy, time-scales dependent features, entropy rate, sliding-window analysis

1. Introduction

Context. Monitoring fetal heart rate (FHR) during labor is a common clinical routine worldwide, aiming to assess fetal well-being and ensure safe delivery. The main objective is to decide on timely operative delivery or uterine relaxation to prevent brain injury and adverse outcomes [9]. In clinical practice, fetal well-being is assessed by obstetricians principally by visual inspection of cardiotocograms (CTG, bivariate time series of beat-per-minute FHR and uterine activity). The interpretation is guided by a set of rules combining a collection of features, aiming to probe various aspects of the CTG, such as baseline FHR, FHR variability and deceleration shape and timing as well as the relation of the various FHR features to the patterns of uterine activity. One such set of features and rules was defined by the International Federation of Gynecology and Obstetrics [19, 6]. Applying such procedure has however been documented as yielding significant inter-and intra-observer variability [40], triggering significant efforts to develop computerized and automated assessment of FHR patterns during labor. Beyond the direct computation of the FIGO features themselves (cf., e.g., [47, 58, 46]), from digitized CTG usually sampled at 4Hz in clinical practice, a large variety of features stemming from advanced signal processing and information theory tools has been computed for FHR assessment. These advanced features, however, have not reached performance benchmarks to lead to a consensus in the research and medical communities. Additionally, performance assessment has mostly been based on immediate post-birth umbilical cord pH measurements, as the ground truth metrics for fetal well-being. However, it has been documented that fetal brain injury poorly correlates with measures of acidemia at birth such as pH [8]. These observations leave open a significant number of issues ranging from the choice of relevant FHR features and the construction of decision rules for such features to the assessment of the relationships between FHR time series and fetal well-being. Interested readers are referred to [29] (and references therein) for a recent (lack of) consensus overview and the interdisciplinary discussions.

Related works. Following achievements in adults and the seminal contribution in [3], frequency-based features were used to model linear temporal dynamics in FHR [57, 35, 63, 45, 56]. To permit richer descriptions of the non-linear dynamics of FHR, information theoretic quantities were used such as entropy rates [12, 18, 50, 61, 37], as well as several nonlinear transforms [44, 45, 10, 30], and scale-free or (multi)fractal paradigms [20, 15, 1, 16]. For overviews, interested readers are referred e.g. [25, 27, 58, 32, 38, 59, 2, 39, 29]. An important limitation in the use of these features lies in their dependence on high quality fetal electrocardiogram (ECG) or magnetocardiogram (MCG) data as input. Such data are not readily available in the majority of clinical settings, with over 90 per cent of North American hospitals, for example, still relying on CTG monitors during labor. CTG however provides FHR at a 4 Hz sampling rate, to be compared to 1000 Hz sampling rate golden standard available with ECG or MCG, while vagally mediated HRV is found on a time scale that goes beyond what is captured at 4 Hz sampling rate. This results in information loss [17, 43, 34, 21].

Beyond the mere design of features and their standalone use, numerous efforts were devoted to devise multiple-feature decision rules, often based on supervised learning and machine learning (cf., e.g.,[7, 11, 64, 31, 58, 13, 64, 65, 28, 60, 2]). Besides the need for large labelled databases to make machine learning effective [28], a recurrent issue is associated with the ground truth being based on pH. This is regularly questioned [29] as, first, pH is only available after delivery hence when FHR is no longer available, and second, brain compromise due to hypoxia-ischemia can ensue when the fetal cerebral blood flow is persistently reduced, e.g. due to precipitous drop in cerebral perfusion pressure resulting from cardiovascular decompensation (CVD) [5, 23]. To better asses the relations between FHR, systemic arterial blood pressure (ABP) and fetal health state sheep were surgically instrumented and subjected to an umbilical cord occlusion (UCO) protocol in [22], in a well-established animal model of human labor. It was observed that the Bezold-Jarisch reflex, a vagal depressor reflex observed in fetal sheep, with worsening acidemia, leads to CVD [24]. This animal model permits to assess relations between FHR and the Bezold-Jarisch reflex mediated vagal sensing of acidemia, a contribution towards the understanding of the links between FHR temporal dynamics and fetal well-being and the central question addressed in the present work.

Goals, contributions and outline. The goal of the present work is to ask whether FHR monitoring can capture the Bezold-Jarisch reflex mediated vagal sensing of acidemia. More particularly, it aims to assess the sensitivity of FHR temporal dynamics, probed by four scale-dependent features, to CVD, metabolites and pH measurements. To that end, it makes uses of the animal model of human labor proposed in [22], where fourteen near-term ovine fetuses subjected to a UCO protocol were instrumented to permit measurements of metabolites, pH and ABP during the UCO mimicking human labor process. Experiments, instrumentation and measurements are described in Section 2. Four features were chosen here essentially because of their being tunable to temporal scales of FHR dynamics preserved at low sampling rate of 4 Hz. This feature choice is also designed to allow computation within short-time time windows, thus permitting to achieve a sliding-window, time-dependent analysis of FHR, which may eventually be exploited to perform real-time and on-line FHR monitoring on noisy FHR data. These features, together with sliding-window analysis are described in Section 3. Results, reported in Section 4, show the sensitivity of the proposed features to UCO strength (cf. Section 4.1), their correlation to metabolites and pH, which may allow for an early acidosis detection (cf. Section 4.2), and the importance of coarse time scales (2.5 to 8seconds) (cf. Section 4.3). Section 4.4 constructs a per-individual self-referencing distance to healthy state based on combination of the four features. The use of the novel composite distance metric to predict CVD from FHR time series alone is reported in Section 4.5.

2. Materials: sheep animal model and umbilical cord occlusions

Fetal sheep model of labor and surgical preparation. The anesthetic and surgical procedures, postoperative care of the animals and the UCO model

of labor have been previously described [22]. Briefly, fourteen near-term ovine fetuses (123 ± 2 days gestational age (GA), term = 145 days) of the mixed breed were surgically instrumented. Animal care followed the guidelines of the Canadian Council on Animal Care and was approved by the University of Western Ontario Council on Animal Care.

Polyvinyl catheters were placed in the right and left brachiocephalic arteries, the cephalic vein, and the amniotic cavity. Stainless steel electrodes were sewn onto the fetal chest to monitor ECG. A polyvinyl catheter was also placed in the maternal femoral vein. Stainless steel electrodes were additionally implanted biparietally on the dura for the recording of electrocorticogram, ECOG, as a measure of summated brain electrical activity (results reported elsewhere [22]). An inflatable silicon rubber cuff (In Vivo Metric, Healdsburg, CA) for UCO induction was placed around the proximal portion of the umbilical cord and secured to the abdominal skin. Once the fetus was returned to the uterus, a catheter was placed in the amniotic fluid cavity. Antibiotics were administered intravenously to the mother (0.2 g of trimethoprim and 1.2 g sulfadoxine, Schering Canada Inc., Pointe-Claire, Canada) and fetus and into the amniotic cavity (1 million IU penicillin G sodium, Pharmaceutical Partners of Canada, Richmond Hill, Canada). Amniotic fluid lost during surgery was replaced with warm saline. The uterus and abdominal wall incisions were sutured in layers and the catheters exteriorized through the maternal flank and secured to the back of the ewe in a plastic pouch. Postoperatively, animals were allowed four days to recover prior to experimentation and daily antibiotic administration was continued intravenously to the mother (0.2 g trimethoprim and 1.2 g sulfadoxine), into the fetal vein and the amniotic cavity (1 million IU penicillin G sodium, respectively). Arterial blood was sampled for evaluation of the fetal condition and catheters were flushed with heparinized saline to maintain patency. Animals were 130 ± 1 day GA on the first day of the experimental study.

Umbilical cord occlusion protocol. All animals were studied over a ~6 hour period. Fetal chronic hypoxia was defined as arterial O₂Sat less than 55 percent as measured on postoperative days 1 to 3 and at baseline prior to beginning the UCOs. The first group comprised five fetuses that were also spontaneously hypoxic (n=5, H/UCO). The second group of fetuses was normoxic (O₂Sat more than 55 percent before UCOs) (n=9, N/UCO). As reported, after a 1-2 hour baseline control period, the animals underwent mild, moderate, and severe series of repetitive UCOs by graduated inflation of the occluder cuff with a saline solution [22].

During the first hour following the baseline period, mild variable FHR decelerations were performed with a partial UCO for 1 minute duration every 2.5 minutes, with the goal of decreasing FHR by ~30 bpm, corresponding to a ~50 percent reduction in umbilical blood flow [41, 52]. During the second hour, moderate variable FHR decelerations were performed with increased partial UCO for 1 minute duration every 2.5 minutes with the goal of decreasing FHR by ~60 bpm, corresponding to a ~75 percent reduction in umbilical blood flow. Animals underwent severe variable FHR decelerations with complete UCO for 1 minute duration every 2.5 minutes until the targeted fetal arterial pH of less

than 7.0 was detected or 2 hours of severe UCO had been carried out, at which point the repetitive UCO were terminated. These animals were then allowed to recover for 48 hours following the last UCO. Fetal arterial blood samples were drawn at baseline, at the end of the first UCO of each series (mild, moderate, severe), and at 20 minute intervals (between UCO) throughout each of the series, as well as at 1, 24, and 48 hours of recovery. For each UCO series, blood gas sample and the 24h recovery sample of 0.7 ml of fetal blood were drawn, while 4 ml of fetal blood were drawn at baseline, at $\text{pH}_{\text{nadir}} < 7.00$, and at 1 hour and 48 hours of recovery. The amounts of blood drawn were documented for each fetus and replaced with an equivalent volume of maternal blood at the end of day 1 of the study. All blood samples were analyzed for blood gas values, pH, lactate and base excess (BE) with an ABL-725 blood gas analyzer (Radiometer Medical, Copenhagen, Denmark) with temperature corrected to 39.0°C. Plasma from the 4 ml blood samples was frozen and stored for cytokine analysis, reported elsewhere. After the 48 hours recovery blood sample, the ewe and the fetus were killed by an overdose of barbiturate (30 mg sodium pentobarbital IV, MTC Pharmaceuticals, Cambridge, Canada). A post mortem was carried out during which fetal sex and weight were determined and the location and function of the umbilical occluder were confirmed. The fetal brain was perfusion-fixed and subsequently dissected and processed for later immunohistochemical study [51].

Data acquisition and pre-processing. A computerized data acquisition system was used to record fetal systemic arterial and amniotic pressures and the ECG signal [17]. All signals were monitored continuously throughout the experiment. Arterial and amniotic pressures were measured using Statham pressure transducers (P23 ID; Gould Inc., Oxnard, CA). Fetal systemic ABP was determined as the difference between instantaneous values of arterial and amniotic pressures. A PowerLab system was used for data acquisition and analysis (Chart 5 For Windows, ADInstruments Pty Ltd, Castile Hill, Australia). Pressures, ECOG and ECG were recorded and digitized at 1000 Hz for further study. For ECG, a 60 Hz notch filter was applied. R peaks of ECG were used to derive the heart rate variability (HRV) times series [17]. The time series of R-R peak intervals were then uniformly resampled at 4 Hz [17]. A representative FHR signal is shown in Fig. 1a: FHR variability increases with the rising UCO strength.

Fetal cardiovascular decompensation. During UCO, by visual inspection, we noted the individual time point at which three successive hypotensive ABP responses to UCO-triggered FHR decelerations occurred. We refer to this time point as the ABP sentinel corresponding to the timing of CVD. We also computed the difference delta between the ABP sentinel and the time when pH_{nadir} (below 7.00) is reached in each fetus. For illustration, the ABP sentinel is depicted using a black vertical line in Figure 1.

Metabolites data (pH, lactate and BE) is obtained by blood sampling performed at specific times during the experiment (vertical lines in 1). In order to have metabolites data at any time, we assume a linear drift between two successive measurements and consequently interpolate between two measurements

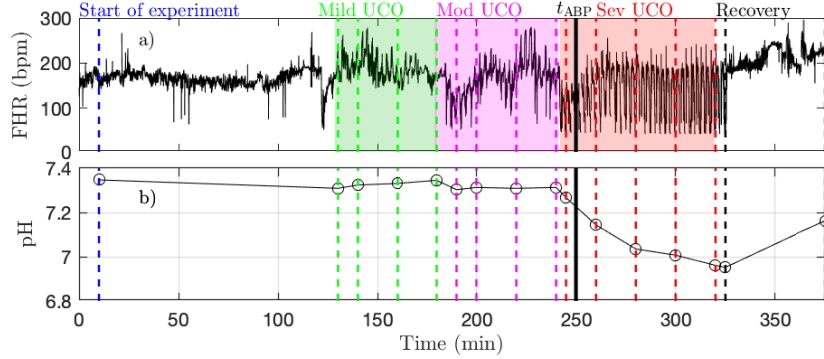


Figure 1: Typical data recorded in the experiment. Up: FHR resampled at 4Hz. The color indicates the intensity of UCO during the experiment: blue and black for no UCO (baseline and recovery), green for mild UCO, magenta for moderate UCO and red for severe UCO. Down: Fetal arterial pH values during the experiment. The pH (as well as the other blood measurements) is obtained at specific time points, indicated by the vertical lines; the open black circles correspond to the actual measurements from blood sampling and the black lines correspond to a linear interpolation.

times. We thus obtain a piece-wise linear time series sampled at 4Hz, depicted in Figure 1b as a black curve.

3. Methods: time scale-dependent features

3.1. Sliding window analysis

Analysis of FHR and metabolites data are performed in sliding time-windows of size $T = 20$ minutes. The time-windows are shifted by $dT = 5$ minutes, thus implying a $T - dT = 15$ minutes (75%) overlap. The k -th time-window thus corresponds to time ranging in $[kdT, kdT + T]$. This sliding window analysis permits the assessment of the temporal evolution of cardiovascular responses to changes in UCO intensity.

3.2. Scale dependent features

Using FHR, x_t , four quantities, whose definitions rely on the choice of a time scale τ , are computed, for each time-window k : increment mean $m_k(\tau)$, increment standard deviation $\sigma_k(\tau)$, the corresponding Student ratio $R_k(\tau)$, and the entropy rate $h_k(\tau)$. The time evolution of (three of) these four features, along with FHR is shown for illustration purposes in Figure 2 for arbitrarily chosen 20-minute window, time scale τ and animal.

3.2.1. Mean variation (or local trend) at time-scale τ

For all t in window k , the average increment over a time scale τ is computed as:

$$m_t(\tau) = \frac{1}{\tau} \sum_{i=t-\tau+1}^t (x_i - x_{t-\tau}) = \frac{1}{\tau} \sum_{i=t-\tau+1}^t x_i - x_{t-\tau} . \quad (1)$$

These $m_t(\tau)$ are then averaged across window k , for all non-overlapping time-intervals $[(j-1)\tau; j\tau]$:

$$m_k(\tau) = \frac{1}{\lfloor T/\tau \rfloor} \sum_{j=1}^{\lfloor T/\tau \rfloor} m_{kT+j\tau}(\tau) , \quad (2)$$

where $\lfloor T/\tau \rfloor$, the floor of the fraction T/τ , indicates the number of time-intervals of size τ available in the time-window of size T . An illustration of the methodology is given in Figure 2b for the window $k = 0$: values of $m_t(\tau)$ are depicted in black, and the single value $m_k(\tau)$ is represented in red.

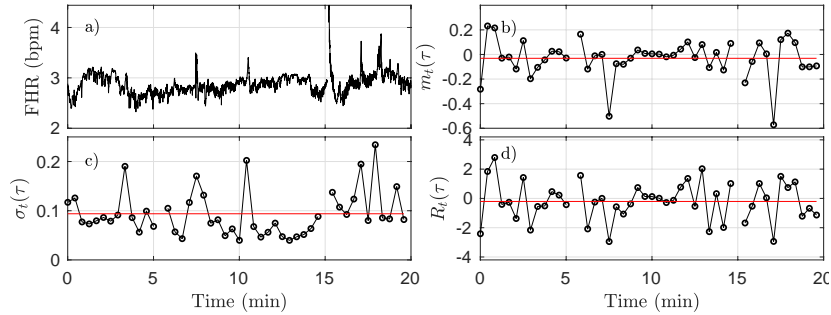


Figure 2: Illustration of the methodology in the first time-window $[0; T]$ of size $T = 20$ minutes, using the fixed time scale $\tau = 25s$. (a): raw FHR. (b): $m_t(\tau)$. (c): $\sigma_t(\tau)$. (d): $R_t(\tau)$. The black circles in (b),(c),(d) correspond each to a value obtained in a time-interval of size $\tau = 25s$, according to eqs (1),(3),(5). The horizontal red lines in (b), (c), (d) indicate the values $m_{k=1}(\tau)$, $\sigma_{k=1}(\tau)$ and $R_{k=1}(\tau)$ obtained after averaging all the black circles, i.e., over all available time-intervals of size τ , according to eqs (2),(4),(6).

The quantity $m_k(\tau)$ measures the average variation — either an increase or a decrease — of FHR on the time scale τ , the average being computed over the k th time-window of size T according to (2).

3.2.2. Standard deviation at time-scale τ

Given a time-interval $[t-\tau; t]$, we define the variance of the set of increments $\{(x_{t-i} - x_{t-\tau}), t-\tau < i \leq t\}$. This indeed is nothing but the variance of x_t , computed over the set of values in the time-interval $[t-\tau; t]$:

$$\sigma_t^2(\tau) = \frac{1}{\tau} \sum_{i=t-\tau+1}^t x_i^2 - \left(\frac{1}{\tau} \sum_{i=t-\tau+1}^t x_i \right)^2 . \quad (3)$$

We then average its square root over the $\lfloor T/\tau \rfloor$ non-overlapping time intervals of size τ available in the k th time-window of size T :

$$\sigma_k(\tau) = \frac{1}{\lfloor T/\tau \rfloor} \sum_{j=1}^{\lfloor T/\tau \rfloor} \sigma_{kT+j\tau}(\tau). \quad (4)$$

This quantity measures the average — in the k th time-window of size T — amplitude of the fluctuations of x_t over τ consecutive points. The methodology is illustrated in Figure 2c.

3.2.3. Normalized local trend at time-scale τ

The Student ratio, or normalized local trend, at time-scale τ , is defined for each time interval $[t - \tau; t]$, as:

$$R_t(\tau) = \frac{m_t(\tau)}{\sigma_t(\tau)}. \quad (5)$$

It is averaged across all available non-overlapping intervals in the k th time-window:

$$R_k(\tau) = \frac{1}{\lfloor T/\tau \rfloor} \sum_{j=1}^{\lfloor T/\tau \rfloor} R_{kT+j\tau}(\tau). \quad (6)$$

This quantity, up to a factor $\sqrt{\tau}$, would correspond to a random variable drawn from the distribution of the t -value if the data x_t were independently drawn from a Gaussian distribution. It can be interpreted as the average variation over a time step τ , normalized by the local standard deviation; as such, it provides a normalized measure of the trend of the signal x_t to depart from its expected value when observed across a duration τ .

3.2.4. Entropy rate at time-scale τ

One commonly used feature in heart rate analysis, both for adults and fetuses, is sample entropy (SampEn) [53, 54, 42], an elaboration on approximate entropy (ApEn) [49, 48]. It was shown recently that the entropy rate provides a related tool to probe FHR with better performance than ApEn or SampEn to detect acidosis [62, 37, 36].

The entropy rate of order 1 in the k th time-window at time-scale τ is defined as:

$$h_k(\tau) = H(x_t, x_{t-\tau}) - H(x_t), \quad (7)$$

where

$$H(\vec{x}) = - \int p(\vec{x}) \ln p(\vec{x}) d\vec{x}, \quad (8)$$

denotes the Shannon entropy [55] of either a vector $\vec{x} = (x_t, x_{t-\tau})$ or a scalar $\vec{x} = x_t$. $h_k(\tau)$ is computed using all the pairs of points $(x_t, x_{t-\tau})$ available in the k -th time-window, and following Theiler's prescription [37] to avoid spurious correlation.

$h_k(\tau)$ measures the extra information conveyed by the vector $(x_t, x_{t-\tau})$ when (x_t) is known, or in other words, the extra information given by the knowledge of the signal at an earlier time $t - \tau$. The entropy rate probes the dynamics of the signal, and to better focus on this dynamical aspect, we compute it on the normalized signal $(x_t - \langle x_t \rangle)/\sqrt{\langle (x_t - \langle x_t \rangle)^2 \rangle}$, where $\langle \cdot \rangle$ stands for the time average on the window of size T .

4. Results and discussion: Features, time-scales and distance to healthy state

In section 4.1, the four features — computed in overlapping time-windows — evolution in time are firstly presented and studied with respect to their relations to UCO intensity. Because these features are computed at a given time-scale τ , they offer a description of the FHR dynamics at this time-scale. We thus explore the correlation between the features at a given time-scale τ and the measured values of the metabolites — including the pH. This global analysis, presented in section 4.2, is performed using all available time-windows and all available animals. We then reduce the dimensionality of the analysis by averaging results over the long-term time-scales, as defined and presented in section 4.3. This allows us to examine more clearly how the features evolve jointly with the UCO intensity for the entire cohort, while quantifying the variability between animals. We then examine quantitatively in section 4.4 how these long-term features correlate with metabolites. We then combine them in an appropriately normalized vector; we are then able to describe the large variability across the subjects in the population as the variability of this vector in the early stages of the experiments. This allows us to define a measure of the degradation of the health state of an animal as the distance from healthy state. Finally, we propose in section 4.5 to use this "individual" distance as a novel indicator — or sentinel — to alert for the degradation of the health status due to CVD. We also show that this indicator/sentinel matches very well with pH measurements.

4.1. Features and UCO strength

We first examine on a single animal how the four FHR features evolve throughout an experiment, depending on the time-scale τ . The values obtained in the k -th time-window $[kdT; kdT + T]$ are assigned to the date $t_k = kdT + T/2$ at the center of the time-window. The dynamical evolutions of $m_k(\tau)$, $\sigma_k(\tau)$, $R_k(\tau)$ and $h_k(t, \tau)$ are depicted in Figure 3 for a large band of time scales τ .

Such a time-scale representation reveals qualitatively that when the UCO strength is increased, $m_k(\tau)$, $R_k(\tau)$ and $h_k(\tau)$ decrease along time, while $\sigma_k(\tau)$ increases along time. This agrees with the previous studies where the decrease of the entropy rate $h_k(\tau)$ was associated with fetal acidosis [62, 36, 37].

Qualitatively, although the four features barely evolve in time for smaller values of τ (below 2 seconds, bottom of the images in Fig. 3), a noticeable time evolution can be observed for large values of τ and especially in the severe UCO regime. To better observe the dependence of the four features on the scale τ ,

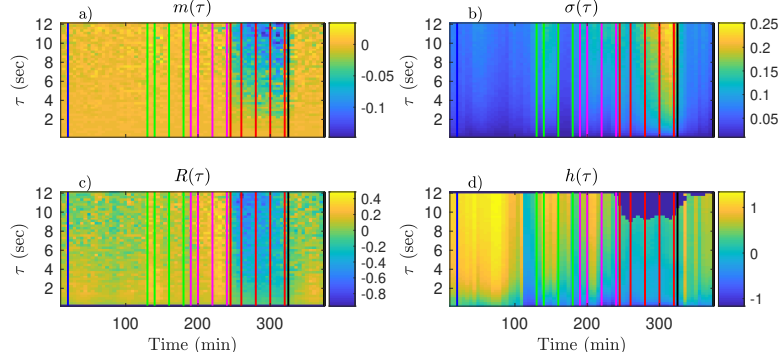


Figure 3: Representation of the time evolutions of $m_k(\tau)$, $\sigma_k(\tau)$, $R_k(\tau)$, $h_k(\tau)$, depending on the scale τ . The time in abscissa is $kdT + T/2$, the location of the k th time-window of size T where the quantity is computed, and the ordinate represents the scale τ . Vertical color lines indicates the times at which blood sampling was performed (same color code as in Fig. 1: green in the mild UCO regime, magenta in the moderate UCO regime, and red in the severe UCO regime). In the severe UCO regime and for larger time scales τ , stronger variations are observed.

we plot in Fig. 4 their evolution with τ for the time points when blood sampling was performed. Fig. 4 therefore presents the evolution of the four features along the vertical color lines indicated in the images of Fig. 3.

We observe in Figure 4 that the evolution of $m_k(\tau)$ is rather linear in τ , but the slope depends on the time, and hence on the UCO level. We observe almost no evolution of $R(\tau)$ with τ , but the value of $R(\tau)$ depends on time, so on the UCO level. On the contrary, both $\sigma(\tau)$ and the entropy rate $h(\tau)$ present a distinct change of their evolution with τ below and above $\tau = 2.5$ s, which emphasizes the distinction between short (< 2.5 seconds) and large (> 2.5 seconds) time scales, in accordance with previous literature [26, 14, 17]. We use this information on the time scales as follows.

4.2. FHR features, arterial metabolites and pH

We now examine, for a fixed time-scale τ , how the features relate to the health state of the animal, as described by the metabolites and pH. To do so, we use all time-windows of size T on one side, and interpolated metabolites data on the other side. We compute the correlation between any of the four features (for a fixed τ) and any of the biochemical measurements, by averaging over all time-windows (average over k) and over all animals. Results are plotted in Fig. 5 as a function of the scale τ .

As suggested by Fig. 4 and confirmed by Fig. 5, we can isolate two bands of time scales: shorter scales $\tau < 2.5$ s (i.e., high frequency band, above 0.4 Hz, short term time scales, labeled ST) and larger ones $\tau > 2.5$ s (low frequency band, below 0.4 Hz, long term time scales, labeled LT).

For any of the four features and any of the three biochemical measurements, the correlation in the range [2.5 – 8] seconds is not only the largest — in abso-

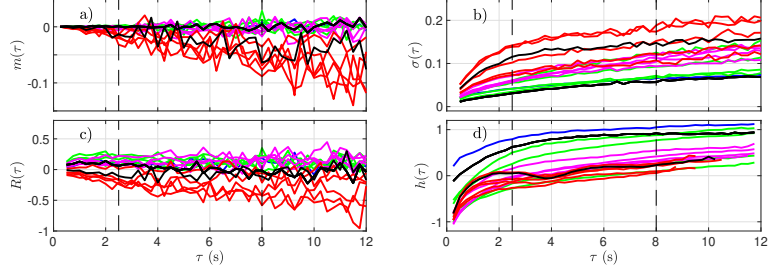


Figure 4: Quantitative representation of the evolution of $m(\tau)$, $\sigma(\tau)$, $R(\tau)$, $h(\tau)$ over the time scale τ for a single animal. The data represented here is extracted from Fig.3: each curve corresponds to a time-window of size T for which a fetal arterial blood sample was taken. The color of the curve represents the corresponding UCO level, with the same color code as in Figures 1 and 3: blue is the baseline prior to any UCO, green in the mild UCO regime, magenta in the moderate UCO regime, red in the severe UCO regime, and then black in the recovery regime (after UCO). Vertical black dashed lines indicate the time-scales 2.5s and 8s.

lute value — but also the most stable: it fluctuates less and does not depend much on τ . Above 8s, all correlations decrease in absolute value, which may be attributed in part to poorer statistics: the number $[T/\tau]$ of available time-intervals of size τ in a time-window of size T decreases, which impacts the averages, see, e.g., equation (2)). As a consequence, we choose in the following to restrict the long term (LT) range to $\tau \leq 8$ s in order to have enough statistical power.

4.3. Long-term scales averaged FHR features

For the sake of simplicity, we now eliminate the dependencies of our features on τ and focus on the LT range. To do so, we compute the area under the

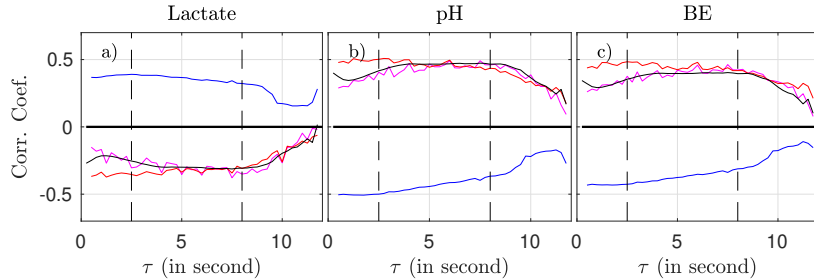


Figure 5: Correlation coefficient between the biochemical measurements (a: lactate, b: pH, c: BE) and the four FHR features: $m_k(\tau)$ (magenta), $\sigma_k(\tau)$ (blue), $R_k(\tau)$ (red), and entropy rate $h_k(\tau)$ (black), as function of the scale τ .

curve (AUC) of our four FHR features in the range $2.5 < \tau < 8\text{s}$. For a given time-window indexed by k , we compute:

$$m_k^{\text{LT}} = \sum_{\tau=2.5\text{s}}^{\tau=8\text{s}} m_k(\tau) \quad (9)$$

and we define accordingly σ_k^{LT} , R_k^{LT} and h_k^{LT} . These features depend only on time, via the index k of the time-window in which they are computed.

Time evolutions of these four LT features are depicted in Fig. 6 for the complete set of 14 animals. Note that for some animals, due to fluctuations in the experimental conditions, there may be less consecutive time-windows of size T available than expected in a given UCO region, and we have then chosen to assign the dark blue color (arbitrary) for the quantity in that situation — see, e.g., the second line (a hypoxic animal), where no data is available in the mild UCO region, and only 4 windows are available in the severe UCO region.

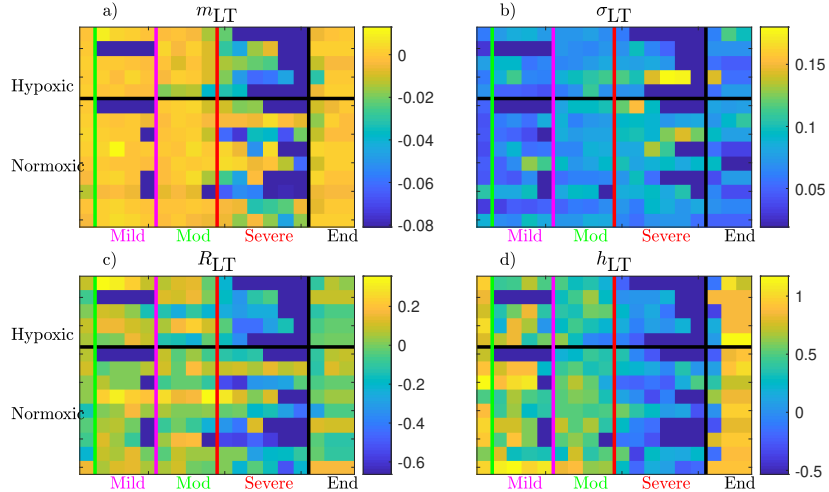


Figure 6: Long term AUC of the four FHR features m_{LT} , σ_{LT} , R_{LT} and h_{LT} for all 14 animals. For a given quantity, each line represents an animal; chronically hypoxic ones are above and normoxic ones are below. Each column represent a time-window of size T and time is increasing from left to right. The region of mild UCO starts at the vertical green line and lasts for 4 windows, up to the vertical magenta line, followed by 4 windows in the moderate UCO region, and then up to 6 windows in the severe UCO region, and up to 3 windows in the recovery region.

Using the first column (on the left of the vertical green line) of each subfigure as a reference, we observe that every quantity evolves as the UCO strength is increased. Although very few changes are observed in the mild UCO region,

much larger variations are observed in the severe UCO region. After the stopping of UCOs (on the right of the vertical black line), we observe that the four features seem to regain their original value, which we interpret as indicating the recovery of the animal, typically after 1 window of size T , so typically 20 minutes after the end of UCOs.

4.4. Distance to healthy state, metabolites and pH

We now explore how our four FHR features relate to the metabolites' levels, and especially to the pH value, which is a widely used indicator of the fetal health status. We report in Table 1 the correlation coefficient between each of the four features m_{LT} , σ_{LT} , R_{LT} and h_{LT} on one hand, and the three biochemical measurements pH, BE and lactate on the other hand. To increase the statistical power, we use all available time-windows of size T and so all linearly interpolated values of the three biochemical measurements.

We observe that the four FHR features correlate well with the pH and BE, while the correlation with the lactate is smaller. All features but σ_{LT} — the LT amplitude of fluctuations — have a correlation coefficient with pH that is at least 0.50, and a correlation coefficient with BE that is at least 0.43. This is interesting, as R_{LT} appears strongly correlated with m_{LT} while relatively uncorrelated with σ_{LT} .

	m_{LT}	σ_{LT}	R_{LT}	h_{LT}	$ \vec{u} $	D	pH	BE	Lactate
m_{LT}	1.00	-0.51	0.77	0.60	0.29	-0.87	0.53	0.48	-0.36
σ_{LT}	-0.51	1.00	-0.19	-0.43	-0.35	0.61	-0.42	-0.36	0.35
R_{LT}	0.77	-0.19	1.00	0.42	0.14	-0.63	0.50	0.48	-0.35
h_{LT}	0.60	-0.43	0.42	1.00	0.89	-0.76	0.50	0.43	-0.32
norm $ \vec{u} $	0.29	-0.35	0.14	0.89	1.00	-0.50	0.35	0.29	-0.21
distance D	-0.87	0.61	-0.63	-0.76	-0.50	1.00	-0.61	-0.53	0.44
pH	0.53	-0.42	0.50	0.50	0.35	-0.61	1.00	0.95	-0.77
BE	0.48	-0.36	0.48	0.43	0.29	-0.53	0.95	1.00	-0.72
Lactate	-0.36	0.35	-0.35	-0.33	-0.21	0.44	-0.77	-0.72	1.00

Table 1: Correlation coefficients between the four individual features, their vectorial combinations, and the three measurements pH, BE and Lactate. Data from all 14 animals and all available time-windows were used.

We believe that each of the four FHR features contributes a particular piece of information about FHR and we therefore aggregate them as follows. For a

single animal and a single time-window indexed by k , we consider the vector

$$\vec{u}_k = \left(\frac{m_k^{\text{LT}}}{m_{\text{RMS}}^{\text{LT}}}, \frac{\sigma_k^{\text{LT}}}{\sigma_{\text{RMS}}^{\text{LT}}}, \frac{R_k^{\text{LT}}}{R_{\text{RMS}}^{\text{LT}}}, \frac{h_k^{\text{LT}}}{h_{\text{RMS}}^{\text{LT}}} \right), \quad (10)$$

where each component is normalized by its standard deviation computed over all animals and over all available time-windows of size T . The four values $(m_{\text{LT}}^{\text{RMS}}, \sigma_{\text{LT}}^{\text{RMS}}, R_{\text{LT}}^{\text{RMS}}, h_{\text{LT}}^{\text{RMS}})$ used for this normalization are hence the same for all animals and all time-windows; they are reproduced in the third line of Table 2.

For a given animal and for a given time-window indexed by k , we use the \mathcal{L}^2 norm in \mathbb{R}^4 to project any vector \vec{u}_k into a positive real number $\|\vec{u}_k\|$ as follows. For each animal, we assume it is in a healthy condition when the experiment is started (so the FHR is fluctuating around the baseline) and we use the first time window of size T as a reference. We thus define the distance between \vec{u}_k which describes the state in the k -th time-window and \vec{u}_0 which describes the state in the first time-window $[0; T]$:

$$D_k = \|\vec{u}_k - \vec{u}_0\|. \quad (11)$$

We interpret this distance D_k for a single animal as a measure of the deviation from the animal's "healthy" state during the experiment.

We report in Table 2 global statistics — obtained by considering all animals — of the four FHR features used as the four components of the vector \vec{u}_t .

	m_{LT}	σ_{LT}	R_{LT}	h_{LT}
mean, over animals and over k	-0.0067	0.0688	-0.0262	0.5957
mean, over animals, fixed $k = 0$	-0.0009	0.0579	0.0128	0.8811
std, over animals and over k	0.0155	0.0282	0.1630	0.4127
std, over animals, fixed $k = 0$	0.0040	0.0221	0.1082	0.1970

Table 2: Means and standard deviations (std) of the four FHR features over the population of 14 animals. First and third lines: averages over animals and over time-windows (k). Second and fourth lines: averages over animals, using the first ($k = 0$) time-window $[0; T]$ only.

The third line of Table 2 reports the values $m_{\text{RMS}}^{\text{LT}}, \sigma_{\text{RMS}}^{\text{LT}}, R_{\text{RMS}}^{\text{LT}}$ and $h_{\text{RMS}}^{\text{LT}}$ used to normalize the vector \vec{u}_k . Their amplitude is notably different, and the normalization is necessary to ensure that each component of \vec{u}_k contributes equally to its norm $\|\vec{u}_k\|$. Whereas this normalization uses all available data (using all times and all animals at once), it is important to stress that we have accounted for the large variability from one animal to another by defining D_k with a reference relative to the very animal under consideration. The variability of the reference point can be seen in the fourth line of Table 2: it accounts for a

large part of the RMS values used in the normalization. Comparing the first two lines of table 2 brings an additional observation leading to the same conclusion: the position of the healthy state \vec{u}_0 is on average over the animals (second line of the table) sensibly different from the position of \vec{u}_k averaged over all animals and all times (first line of table). Using D_k instead of $\|\vec{u}_k\|$ removes a large part of the inter-animal variability and definitely improves the relevance of the distance, as measured by the correlation with the metabolites, see table 1.

We present in Figure 7 the 14 trajectories of the vector $\vec{u}(k)$ for the complete cohort. Although the trajectories wander in a large region of the phase space, their color-coding seem to only depend on the distance from the origin. During

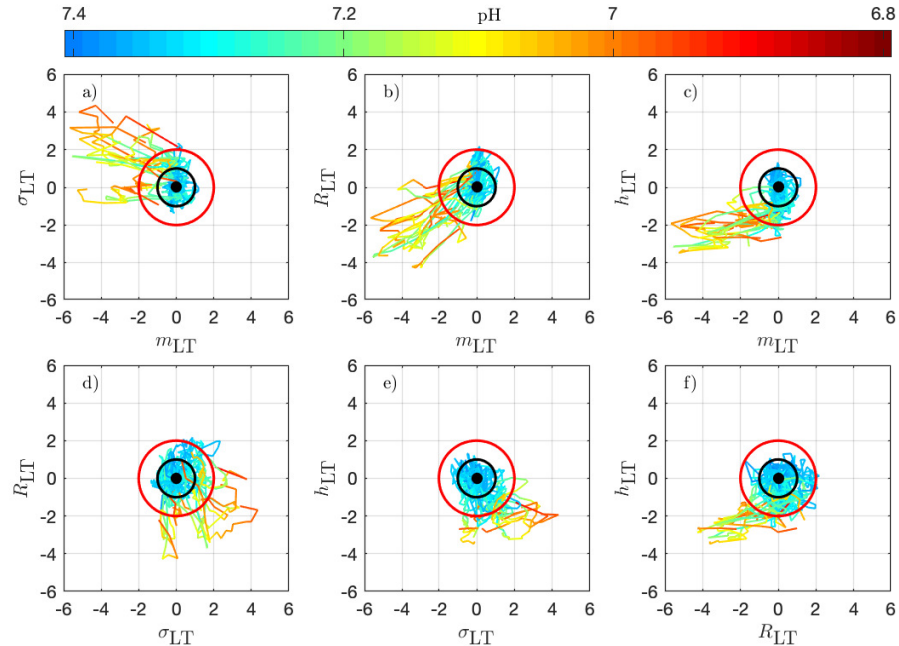


Figure 7: Trajectories of the vector $\vec{u}_k - \vec{u}_0$ for all 14 animals in the phase space; the 6 subplots correspond to the 6 possible projections onto planes (using 2 coordinates of the vector). Each trajectory corresponds to an animal and is colored to indicate the pH value at the time k : in this way, we observe the joint temporal evolution of \vec{u}_k and of the pH throughout the experiment. Trajectories have been centered by subtracting \vec{u}_0 , according to eq.(11) to account for the variability between animals: the thick black dot at the origin, therefore, represents the starting point of all trajectories. The black circle corresponds to $D = 1$ and the red circle to $D = 2$.

an experiment, the UCO's strength increases and, as a consequence, the pH decreases. We observe that the distance D_k appears to increase concomitantly, and more precisely we observe its correlation with the pH value. The correlation coefficients between the distance D and the biochemical measurements, computed over all animals, are reported in Table 1 (grey-colored cells). We

observe that among all FHR features we have computed, the distance D is the one that is the most correlated with pH, as well as with the other metabolites. This confirms that using all four FHR features simultaneously — by considering the vector \vec{u} — not only mitigates the various evolutions of single features with the metabolite value but also aggregates their correlations.

4.5. Distance to healthy state as a new sentinel for CVD

To better illustrate the relation between the dynamical features — especially the distance D_k — on one hand, and the health status as assessed by the metabolites — especially the pH — and blood pressure responses to UCOs on the other hand, we examine in detail how these are co-evolving for each individual animal.

Figure 8 presents the evolutions of \vec{u}_k for two typical normoxic animals. From now on, we discard any indication of the UCO level, and only focus on the trajectory of D_k which we color-code using the pH value, as in Figure 7.

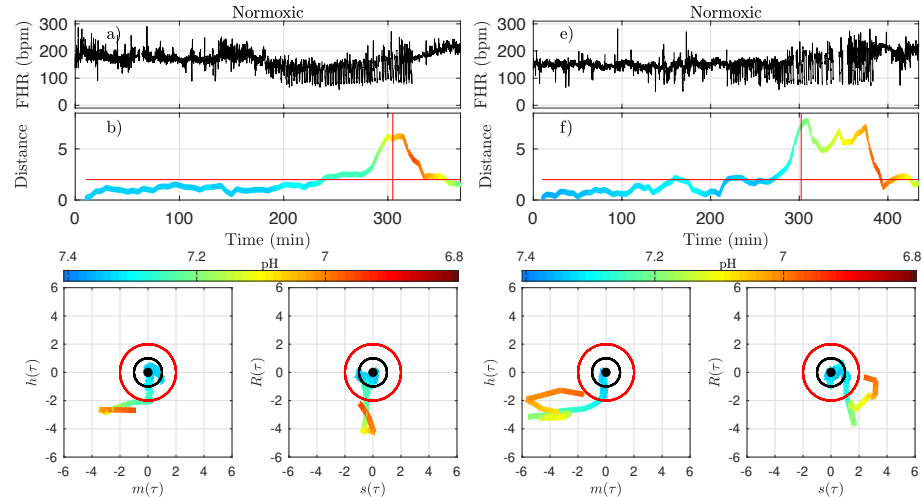


Figure 8: Two examples of normoxic animals (right and left). Upper part: FHR, together with the distance D computed over time. Lower part: Projections of the trajectory of the vector \vec{u} in left: the plane (m_{LT}, h_{LT}) (the two features that individually better correlate with the pH) and right: the plane (σ_{LT}, R_{LT}) (the other two components of \vec{u}). The distance D and the trajectories are color-coded with the pH values in each time-window of size T . For clarity, only the part of the trajectory where D increases up to its maximal value is represented. The red vertical line in the time-trace of the distance D indicates the ABP sentinel, i.e., the time point when we visually confirm the onset of CVD.

Because the vector \vec{u}_k has been carefully normalized, and appropriately centered to define the distance D_k , this last quantity has no dimension and can be compared to absolute values. The particular value $D = 1$ defines the standard deviation range in a healthy situation and the value $D = 2$ corresponds to variations with an amplitude of 2 standard deviations. Looking at the trajectory

projections, we see that during the early stages of the experiments the distance remains small, albeit fluctuating, as long as the pH value remains close to its normal value (bluish color, indicating a pH close to 7.4). More interestingly, we see that when the pH decreases down to 7.2 (greenish color), the distance usually increases up to 2. Finally, we observe that when $D > 2$, the pH is always pathologically low, which signals that the fetus is in an acidic condition.

The very same observations can be made for hypoxic animals, see Figure 9 for two examples.

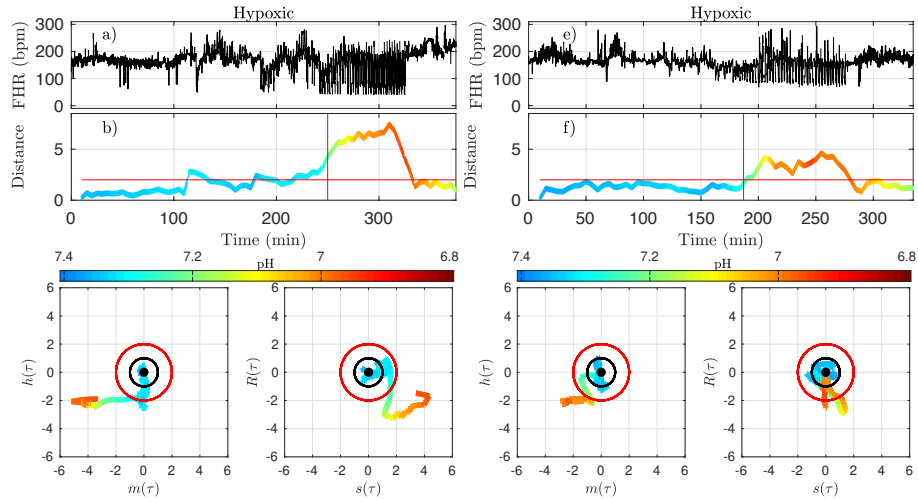


Figure 9: Two examples of hypoxic animals (right and left). Cf. Figure 8. Upper part: FHR, together with the distance D computed over time. Lower part: Projections of the trajectory of the vector \vec{u} in left: the plane (m_{LT}, h_{LT}) (the two features that individually better correlate with the pH) and right: the plane (σ_{LT}, R_{LT}) (the other two components of \vec{u}). The distance D and the trajectories are color-coded with the pH values in each time-window of size T . For clarity, only the part of the trajectory where D increases up to its maximal value is represented. The red vertical line in the time-trace of the distance D indicates the ABP sentinel, i.e., the time point when we visually confirm the onset of CVD.

We now examine quantitatively for each animal the time evolution of the distance from its own reference healthy state. In every time-window $[kdT, kdT + T]$ of size T indexed by k , we have a value D_k which we assign to time $t = kdT + T/2$; we plot the time-evolution of the distance in the upper panels of Figures 8 and 9 with a color that indicates the pH value. This allows for the following interesting observations. First, before the occurrence of UCO, the distance fluctuates with a typical standard deviation of 1. This confirms that the normalization step is valid, albeit it uses values averaged over all animals and all available time-windows. Second, we see that the distance D is substantially larger when UCOs are performed, and more precisely, we see that D increases as the UCO strength is increased or UCOs are being applied to the animal with the same strength but for a longer period of time. As such, the distance D

seems to be a good representation of the health condition of the animal. More interestingly, we showed (table 1) that D is highly correlated with the pH value throughout the complete experiment, but we now observe that a large value of D , above 2, proves to be a very good indicator of a low pH value signaling an acidemia with $\text{pH} < 7.2$.

To further test the ability of the distance D to alert on the fetal condition, we now try to relate the large values of the distance D to the onset of the fetal CVD, i.e., failure of the fetus to mount a hypertensive arterial blood pressure response to UCOs and the UCO-induced FHR decelerations, a prerequisite to maintaining an adequate cerebral perfusion pressure. To do so, we use the so-called ABP sentinel as the reference time when CVD occurs. This sentinel is defined visually as the time when a persistent (over three or more UCO cycles) appearance of pathological hypotensive blood pressure response to UCO-induced FHR decelerations is observed [33]. ABP sentinel is obtained by an expert visual analysis and offers a valuable benchmark for an early detection of hypotensive blood pressure response. As an illustration, the time given by the ABP sentinel is reported in Figure 1b as a vertical black line, and in Figure 8b,f and Figure 9b,f as a vertical red line.

ABP sentinel appears on group average for a pH of 7.20 and 60 minutes prior to pH_{nadir} of less than 7.00, but shows a considerable inter-individual spread. Here we see on phase-space projections in Figures 8c,d and 9c,d that the criterion $D \geq 2$ offers a similar early alert on the deterioration of the animal condition with regard to CVD timing. Looking at either the phase space representation or the time traces of the distance D , we see that this quantity evolves continuously in time, on typical time-scales larger than 20 minutes, the duration we have chosen to compute our quantity. The distance increases over the duration of the experiment and one can easily measure the time t_D at which D crosses the value $D = 2$ (red circle or horizontal line in Figures 8 and 9). Unfortunately, the distance D is very sensitive and it can be seen on the examples that it is possible for D to reach values larger than 2 early in the experiment. We interpret such events as signaling some blood pressure regulatory difficulties, though we did not push this analysis further. To overcome these events — and, hence, to make our new sentinel less sensitive —, we arbitrarily adjust our criteria and require $D_k > 2.5$ for at least 3 consecutive time-windows, so for a long enough duration of about 40 minutes. Table 3 presents the various timings corresponding to the various UCO regimes for each animal, together with an estimate of the pH nadir time, while table 4 presents a summary of our findings, together with the ABP sentinel (CVD time), the two of them appearing before $\text{pH} \leq 7.00$.

The agreement between the ABP sentinel time and the distance time is very satisfying, knowing that we have arbitrarily reduced the sensitivity of our measure. The difference between t_{ABP} and t_D is always smaller than the difference between t_{pH} and t_{ABP} , and also smaller than 20 minutes, the size of the time-windows we have used.

However, for one animal (number 473360, last line in table 4), a large discrepancy is observed. A closer examination of both the data and our distance measure for this animal is given in Figure 10 and allows us to discuss the sen-

	animal (ID)	UCO start time				pH nadir time t_{pH} (hh:mm:ss)
		mild (hh:mm:ss)	moderate (hh:mm:ss)	severe (hh:mm:ss)	recovery (hh:mm:ss)	
Hypoxic	8003	01:14:14	02:11:11	03:14:14	03:21:21	03:21:21
	473351	NaN	04:08:08	05:16:16	06:40:40	05:51:51
	473362	02:08:08	03:09:09	04:02:02	04:37:37	04:38:38
	473376	02:52:52	03:47:47	04:43:43	05:46:46	05:50:50
	473726	02:09:09	03:09:09	04:04:04	05:26:26	05:25:25
Normoxic	461060	02:58:58	03:52:52	04:57:57	06:29:29	06:29:29
	473361	01:55:55	02:58:58	04:01:01	06:31:31	05:25:25
	473352	NaN	03:58:58	04:58:58	05:44:44	05:37:37
	473377	02:28:28	03:31:31	04:30:30	06:31:31	06:27:27
	473378	03:17:17	04:15:15	05:10:10	05:47:47	05:44:44
	473727	01:37:37	02:42:42	03:39:39	05:47:47	05:18:18
	5054	01:30:30	02:27:27	03:30:30	05:22:22	05:22:22
	5060	01:09:09	02:06:06	03:08:08	04:07:07	04:02:02
	473360	02:11:11	03:16:16	04:13:13	06:10:10	06:10:10

Table 3: The individual onset times for each UCO regime and reaching pH nadir. The UCO regimes mild, moderate, severe and recovery are colored green, magenta and red in Figure 1) pH nadir time t_{pH} (when $pH \leq 7.00$) measured from linear interpolation of pH data (as seen for example in Figure 1b).

sitivity of our measure. We have used the 4Hz FHR dataset which was also studied in earlier literature. This dataset is obtained from the R-R intervals data at 4Hz, which is interpolated from the raw ECG-derived R-R intervals data recorded at 1000Hz. As can be seen in Figure 10, the genuine 1000 Hz dataset (in red) is missing some values during short intervals and the resampling process, which uses splines interpolation, creates arbitrary values for the 4Hz FHR dataset (in black) within such intervals. This results in additional values which exhibit large and fast fluctuations which are non-physiological. Whereas most of these do not impact the value of the distance D (see Figure 10e,f and 10g,h), there is a time interval (at about $t = 172$ s, see Figure 10b,d where D is unexpectedly large, reaching a value around 4. This is concomitant with a sharp drop in FHR, as can be seen in Figure 10a,c. This sharp drop is exacer-

bated on the 4Hz signal compared to the 1000Hz signal, and is very localized in time, which leads to a later decrease of D , contrary to the pathological situation reported in Figure 10g,h where D remains at a large value. As a consequence, we obtain a false positive sentinel time t_D which corresponds to this event and is hence much earlier than the ABP sentinel time, although in agreement with previously reported results using the same 4Hz FHR dataset [34]. We conclude that splines interpolation should be avoided, and we suggest instead not to add or create artificial data points when genuine data is not available. Additionally, each of the quantities we propose, and hence the distance D , can still be computed, as they are all robust with respect to missing data.

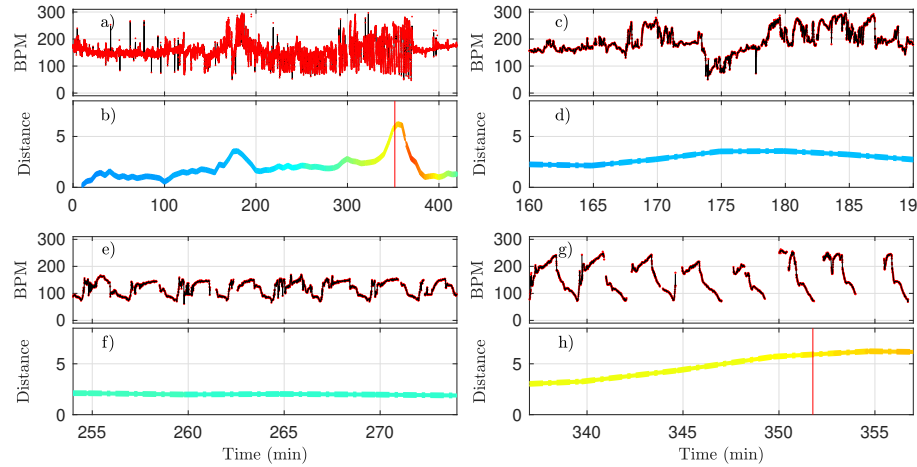


Figure 10: A representative example of FHR and the corresponding distance D (colored by pH value) for animal 473360. The 4Hz dataset used in the analysis is reproduced in black, and the original 1000 Hz dataset is presented in red. a,b : complete time trace for all available data. c,d : zoom in the problematic region, where D is unexpectedly large. e,f : zoom in a region where D is small, as expected. g,h : zoom in a region where D is large, as expected. See text.

A deeper examination of each experiment, using animal's systemic arterial blood pressure data, should clarify the relationship between the increases of the distance from healthy condition and the incipient arterial hypotension. This work is out of scope of the present article which focuses on the dynamics of the clinically relevant 4Hz-sampled FHR signal.

As such, we propose that the distance D has the potential to serve as an individual biomarker of the incipient CVD, *i.e.*, an early sentinel of the fetal brain injury.

5. Conclusions and outlook

In the present work, four FHR features, whose definitions depend on the timescale, are computed on the FHR dataset derived from an animal model of

human labor to quantify the evolution of FHR temporal dynamics as a function of the UCO strength. We also correlated the variations of such timescale-dependent quantities to metabolite and pH measurements. We show the relevance of timescales ranging in $[2.5 - 8]$ seconds (equivalently $[0.125 - 0.4]$ Hz in frequencies) for early detection of both acidemia and CVD, matching the scales classically used in FHR analysis and referred to as long-term [16, 2]. We observed that reduced pH closely relates to larger m_{LT} which may be interpreted as an increase of baseline [59, 2]), and lower entropy rate h_{LT} , in agreement with earlier findings reported in the literature [37]. More importantly, a per-individual distance metric was constructed from these four (population-normalized) features to quantify a self-referencing departure from a healthy state for each subject independently. Such a definition raises two issues. Firstly, it requires, as is often the case, that monitoring is started early enough while the fetus is still in a healthy condition, so as to create a self-reference to normal on a per-individual basis. If fetuses are already in distress when monitoring is initiated, the distance, albeit increasing with distress, may fail to detect CVD correctly. Secondly, the definition of the vector, and hence the distance, requires a normalization, which is performed in the present work at the population level, i.e., using an average across subjects. Although such an average should converge rapidly with the population size, this dependence requires further investigations.

However, the constructed distance proved able to detect accurately the occurrence of acidemia and CVD from the analysis of FHR only, and without recourse to pH. This opens the route to investigating the relevance of such metrics in clinical practice, as it is non-invasive and based on mechanical processes, which are much faster than the biochemical ones underlying the use of pH. Further, for practical purposes, the present studies show that the computation of features and distance is robust to FHR sampled at 4Hz and, to some extent, to missing data. Also, the FHR features and distance are computed in sliding-windows, permitting a on-line and quasi-real time analysis of the evolution of the dynamics of FHR, and thus in relation to a local health state of the fetus. The extent to which the 20-min sliding-window size, chosen here for proof-of-concept developments, can be further reduced to 10 or 5-min, is under investigation. This provides a large therapeutic time window for health practitioners managing the delivery.

It has been documented that sheep fetuses have an individual cardiovascular phenotype in their responses to increasing acidemia due to repetitive intermittent hypoxia [23]. Chronically hypoxic fetuses have diminished cardiovascular defenses to hypotensive stress [4]. We hypothesized that such phenotype would be reflected in individual FHR variability properties. We could not identify any influence of the phenotype (normoxic / hypoxic) in any of the metrics including the distance D . We are currently exploring whether the initial vector \vec{u}_0 may contain such information.

Conflict of Interest Statement

M. G. Frasch has an aECG patent (WO2018160890A1). The authors declare that the research was conducted in the absence of any other commercial or financial relationships that could be construed as a potential conflict of interest.

Author Contributions

S. G. Roux designed the signal processing tools, ensured their practical implementation, conducted their application to data and the analysis and interpretation of the results. He also prepared the figures and tables reported in the article.

N. B. Garnier contributed to the design of the signal processing tools, to the analysis and interpretation of the results and to the writing of the paper.

P. Abry contributed to the interdisciplinary connections between signal processing and medical doctor teams, to the interpretation of the results and to the writing of the paper.

N. Gold contributed to the measurements and the manuscript. He also performed the changepoint-based detection of the cardiovascular decompensation.

M. G. Frasch designed the experiment and conducted the surgeries and measurements. He also performed the expert visual detection of the cardiovascular decompensation used as ground truth here. He contributed to writing the article and to the interpretation of the results.

Funding

Work supported by Grant ANR-16-CE33-0020 MultiFracs.

Acknowledgments

The authors thank the Signal Processing and Monitoring Workshop (SPaM workshop) launched under the umbrella of the ANR French Grant #18535 FE-TUSES where the first stages of the present work were discussed. The authors gratefully acknowledge Dr. Bryan Richardson and his Perinatal Research at the University of Western Ontario for the original design of the animal experiments that enabled the acquisition of the dataset underlying the present study. MGF is funded by the Canadian Institutes for Health Research (CIHR).

References

- [1] ABRY, P., ROUX, S., CHUDÁČEK, V., BORGNAK, P., GONÇALVES, P., AND DORET, M. Hurst Exponent and Intrapartum Fetal Heart Rate: Impact of Decelerations. In 26th International Symposium on Computer-Based Medical Systems (CBMS) (2013), pp. 1–6.

[2] ABRY, P., SPILKA, J., LEONARDUZZI, R., CHUDÁČEK, V., PUSTELNIK, N., AND DORET, M. Sparse learning for intrapartum fetal heart rate analysis. *Biomedical Physics & Engineering Express* 4, 3 (2018), 034002.

[3] AKSELROD, S., GORDON, D., UBEL, F. A., SHANNON, D. C., BERGER, A. C., AND COHEN, R. J. Power spectrum analysis of heart rate fluctuation: a quantitative probe of beat-to-beat cardiovascular control. *Science* 213, 4504 (1981), 220–222.

[4] ALLISON, B. J., BRAIN, K. L., NIU, Y., KANE, A. D., HERRERA, E. A., THAKOR, A. S., BOTTING, K. J., CROSS, C. M., ITANI, N., SHAW, C. J., SKEFFINGTON, K. L., BECK, C., AND GIUSSANI, D. A. Altered cardiovascular defense to hypotensive stress in the chronically hypoxic fetus. *Hypertension* 76, 4 (2020), 1195–1207.

[5] ASTRUP, J. Energy-requiring cell functions in the ischemic brain. their critical supply and possible inhibition in protective therapy. *J Neurosurg* 56, 4 (1982), 482–497.

[6] AYRES-DE CAMPOS, D., SPONG, C. Y., CHANDRAHARAN, E., AND INTRAPARTUM FETAL MONITORING EXPERT CONSENSUS PANEL, F. I. G. O. Figo consensus guidelines on intrapartum fetal monitoring: Cardiotocography. *Int J Gynaecol Obstet* 131, 1 (Oct 2015), 13–24.

[7] BERNARDES, J., MOURA, C., DE SA, J. P., AND LEITE, L. P. The Porto system for automated cardiotocographic signal analysis. *J Perinat Med* 19, 1-2 (1991), 61–65.

[8] CAHILL, A., MATHUR, A., SMYSER, C., AND ET AL. Neurologic injury in academic term infants. *Am J Perinatol* 34, 7 (2017), 668–675.

[9] CHANDRAHARAN, E., AND ARULKUMARAN, S. Prevention of birth asphyxia: responding appropriately to cardiotocograph (CTG) traces. *Best Pract. Res. Clin. Obstet. Gynaecol.* 21, 4 (2007), 609–624.

[10] CHUDÁČEK, V., ANDEN, J., MALLAT, S., ABRY, P., AND DORET, M. Scattering transform for intrapartum fetal heart rate variability fractal analysis: A case-control study. *IEEE Transactions on Biomedical Engineering* 61, 4 (April 2014), 1100–1108.

[11] COSTA, A., AYRES-DE CAMPOS, D., COSTA, F., SANTOS, C., AND BERNARDES, J. Prediction of neonatal acidemia by computer analysis of fetal heart rate and ST event signals. *Am J Obstet Gynecol* 201, 5 (Nov 2009), 464.e1–464.e6.

[12] COSTA, M., GOLDBERGER, A. L., AND PENG, C. K. Multiscale entropy analysis of complex physiologic time series. *Physical Review Letters* 89, 6 (Aug. 2002), 068102.

- [13] CZABANSKI, R., JEZEWSKI, J., MATONIA, A., AND JEZEWSKI, M. Computerized analysis of fetal heart rate signals as the predictor of neonatal acidemia. *Expert Systems with Applications* 39, 15 (2012), 11846–11860.
- [14] DAVID, M., HIRSCH, M., KARIN, J., TOLEDO, E., AND AKSELROD, S. An estimate of fetal autonomic state by time-frequency analysis of fetal heart rate variability. *Journal of Applied Physiology* 102, 3 (2007), 1057–1064. PMID: 17095644.
- [15] DORET, M., HELGASON, H., ABRY, P., GONÇALVÉS, P., GHARIB, C., AND GAUCHERAND, P. Multifractal analysis of fetal heart rate variability in fetuses with and without severe acidosis during labor. *American Journal of Perinatology* 28, 4 (2011), 259–266.
- [16] DORET, M., SPILKA, J., CHUDÁČEK, V., GONÇALVES, P., AND ABRY, P. Fractal Analysis and Hurst Parameter for intrapartum fetal heart rate variability analysis: A versatile alternative to Frequency bands and LF/HF ratio. *PLoS ONE* 10, 8 (08 2015), e0136661.
- [17] DUROSIER, D., GREEN, G., BATKIN, I., SEELY, A. J., ROSS, M. G., RICHARDSON, B. S., AND FRASCH, M. G. Sampling rate of heart rate variability impacts the ability to detect acidemia in ovine fetuses near-term. *Front Pediatr.* 2 (May 2014), 38.
- [18] ECHEVERRIA, J. C., HAYES-GILL, B. R., CROWE, J. A., WOOLFSON, M. S., AND CROAKER, G. D. H. Detrended fluctuation analysis: a suitable method for studying fetal heart rate variability? *Physiol Meas* 25, 3 (Jun 2004), 763–774.
- [19] FIGO. Guidelines for the Use of Fetal Monitoring. *Int J Gynaecol Obstet* 25 (1986), 159–167.
- [20] FRANCIS, D. P., WILLSON, K., GEORGIADOU, P., WENSEL, R., DAVIES, L., COATS, A., AND PIEPOLI, M. Physiological basis of fractal complexity properties of heart rate variability in man. *J Physiol* 542, Pt 2 (Jul 2002), 619–629.
- [21] FRASCH, M. Heart rate variability code: Does it exist and can we hack it?, 2020.
- [22] FRASCH, M., DUROSIER, L., GOLD, N., CAO, M., MATUSHEWSKI, B., KEENLISIDE, L., Y., L., ROSS, M., AND RICHARDSON, B. Adaptive shutdown of eeg activity predicts critical acidemia in the near-term ovine fetus. *Physiological Reports* 3, 7 (2015), 129A.
- [23] FRASCH, M., KEEN, A., GAGNON, R., ROSS, M., AND RICHARDSON, B. Monitoring fetal electrocortical activity during labour for predicting worsening acidemia: a prospective study in the ovine fetus near term. *PLoS One* 6, 7 (2011), e22100.

[24] FRASCH, M., MANSANO, R., ROSS, M., GAGNON, R., AND RICHARDSON, B. Do repetitive umbilical cord occlusions (uco) with worsening acidemia induce the bezold-jarisch reflex (bjr) in the ovine fetus near term? *Reprod Sci* 15, 2 (2008), 129A.

[25] FRASCH, M., MÜLLER, T., HOYER, D., WEISS, C., SCHUBERT, H., AND SCHWAB, M. Nonlinear properties of vagal and sympathetic modulations of heart rate variability in ovine fetus near term. *American journal of physiology. Regulatory, integrative and comparative physiology* 296, 3 (2009), R702–R707.

[26] FRASCH, M., ZWIENER, U., HOYER, D., AND EISELT, M. Autonomic organization of respirocardial function in healthy human neonates in quiet and active sleep. *Early Human Development* 83, 4 (2007), 269 – 277.

[27] FRASCH, M. G., FRANK, B., LAST, M., AND MÜLLER, T. Time scales of autonomic information flow in near-term fetal sheep. *Frontiers in physiology* 3 (2012), 378.

[28] FRASCH, M. G., XU, Y., STAMPALIJA, T., ET AL. Correlating multi-dimensional fetal heart rate variability analysis with acid-base balance at birth. *Physiol meas* 35, 12 (2014), L1.

[29] GEORGIEVA, A., ABRY, P., CHUDÁČEK, V., DJURIĆ, P. M., FRASCH, M. G., KOK, R., LEAR, C. A., LEMMENS, S. N., NUNES, I., PAPAGEORGIOU, A. T., ET AL. Computer-based intrapartum fetal monitoring and beyond: A review of the 2nd workshop on signal processing and monitoring in labor (october 2017, oxford, uk). *Acta obstetricia et gynecologica Scandinavica* 98, 9 (2019), 1207–1217.

[30] GEORGIEVA, A., PAPAGEORGIOU, A. T., PAYNE, S. J., MOULDEN, M., AND REDMAN, C. W. G. Phase-rectified signal averaging for intrapartum electronic fetal heart rate monitoring is related to acidemia at birth. *BJOG* 121, 7 (Jun 2014), 889–894.

[31] GEORGIEVA, A., PAYNE, S. J., MOULDEN, M., AND REDMAN, C. W. G. Artificial neural networks applied to fetal monitoring in labour. *Neural Computing and Applications* 22, 1 (2013), 85–93.

[32] GIERALTOWSKI, J., HOYER, D., TETSCHKE, F., NOWACK, S., SCHNEIDER, U., AND ZEBROWSKI, J. Development of multiscale complexity and multifractality of fetal heart rate variability. *Autonomic neuroscience : basic & clinical* 178, (1-2) (2013), 29–36.

[33] GOLD, N., FRASCH, M. G., HERRY, C. L., RICHARDSON, B. S., AND WANG, X. A doubly stochastic change point detection algorithm for noisy biological signals. *Frontiers in Physiology* 8 (2018), 1112.

[34] GOLD, N., HERRY, C. L., WANG, X., AND FRASCH, M. G. Fetal cardiovascular decompensation during labor predicted from the individual heart rate: a prospective study in fetal sheep near term and the impact of low sampling rate, 2019.

[35] GONÇALVES, H., ROCHA, A. P., DE CAMPOS, D. A., AND BERNARDES, J. Linear and nonlinear fetal heart rate analysis of normal and acidemic fetuses in the minutes preceding delivery. *Med Biol Eng Comput* 44, 10 (Oct 2006), 847–855.

[36] GRANERO-BELINCHON, C., ROUX, S., GARNIER, N., ABRY, P., AND DORET, M. Mutual information for intrapartum fetal heart rate analysis. *Conf. Proc. of the IEEE Eng. Med. Biol. Soc. (EMBC)* (2017), 2014–2017.

[37] GRANERO-BELINCHON, C., ROUX, S. G., ABRY, P., DORET, M., AND GARNIER, N. B. Information theory to probe intrapartum fetal heart rate dynamics. *Entropy* 19 (2017), 640.

[38] HARITOPOULOS, M., ILLANES, A., AND NANDI, A. *Survey on Cardiotocography Feature Extraction Algorithms for Fetal Welfare Assessment*. Springer International Publishing, Cham, 2016, pp. 1187–1192.

[39] HERRY, C., BURNS, P., DESROCHERS, A., FECTEAU, G., DUROSIER, L., CAO, M., SEELY, A., AND FRASCH, M. Vagal contributions to fetal heart rate variability: an omics approach. *Physiological measurement* 40, 6 (2019), 065004.

[40] HRUBAN, L., SPILKA, J., CHUDÁČEK, V., JANKŮ, P., HUPTYCH, M., BURŠA, M., HUDEC, A., KACEROVSKÝ, M., KOUCKÝ, M., PROCHÁZKA, M., KOREČKO, V., SEGETÁ, J., ŠIMETKA, O., MĚCHUROVÁ, A., AND LHOTSKÁ, L. Agreement on intrapartum cardiotocogram recordings between expert obstetricians. *Journal of Evaluation in Clinical Practice* 21, 4 (2015), 694–702.

[41] ITSKOVITZ, J., LAGAMMA, E., AND A.M., R. Heart rate and blood pressure responses to umbilical cord compression in fetal lambs with special reference to the mechanism of variable deceleration. *Am J Obstet Gynecol* 147, 4 (1983), 451–457.

[42] LAKE, D. E., RICHMAN, J. S., GRIFFIN, M. P., AND MOORMAN, J. R. Sample entropy analysis of neonatal heart rate variability. *Am J Physiol Regul Integr Comp Physiol* 283, 3 (Sep 2002), R789–R797.

[43] LI, X., XU, Y., HERRY, C., DUROSIER, L., CASATI, D., STAMPALIJA, T., MAISONNEUVE, E., SEELY, A., AUDIBERT, F., ALFIREVIC, Z., FERRAZZI, E., WANG, X., AND FRASCH, M. Sampling frequency of fetal heart rate impacts the ability to predict pH and BE at birth: a retrospective multi-cohort study. *Physiological measurement* 36, 5 (apr 2015), L1–L12.

[44] MAGENES, G., SIGNORINI, M. G., AND ARDUINI, D. Classification of cardiotocographic records by neural networks. *Proc. IEEE-INNS-ENNS International Joint Conference on Neural Networks (IJCNN)* 3 (2000), 637–641.

[45] MAGENES, G., SIGNORINI, M. G., FERRARIO, M., PEDRINAZZI, L., AND ARDUINI, D. Improving the fetal cardiotocographic monitoring by advanced signal processing. *Conf. proc. of the IEEE Eng. Med. Biol. Soc. (EMBC)* 3 (2003), 2295–2298.

[46] NUNES, I., DE CAMPOS, D. A., UGWUMADU, A., AMIN, P., BANFIELD, P., NICOLL, A., CUNNINGHAM, S., COSTA-SANTOS, P. S. P. C., AND BERNARDES, J. Central fetal monitoring with and without computer analysis: A randomized controlled trial. *Obstet Gynecol.* 129, 1 (2017), 83–90.

[47] PARER, J. T., KING, T., FLANDERS, S., FOX, M., AND KILPATRICK, S. J. Fetal acidemia and electronic fetal heart rate patterns: is there evidence of an association? *J Matern Fetal Neonatal Med* 19, 5 (May 2006), 289–294.

[48] PINCUS, S. Approximate entropy (ApEn) as a complexity measure. *Chaos* 5 (1) (1995), 110–117.

[49] PINCUS, S. M. Approximate entropy as a measure of system-complexity. *Proc. Natl. Acad. Sci. U.S.A.* 88, 6 (Mar. 1991), 2297–2301.

[50] PORTA, A., BARI, V., BASSANI, T., MARCHI, A., TASSIN, S., CANESI, M., BARBIC, F., AND FURLAN, R. Entropy-based complexity of the cardiovascular control in parkinson disease: Comparison between binning and k-nearest-neighbor approaches. *Conf Proc IEEE Eng Med Biol Soc (EMBC)* (July 2013), 5045–5048.

[51] PROUT, A., FRASCH, M., VELDHUIZEN, R., HAMMOND, R., ROSS, M., AND B.S., R. Systemic and cerebral inflammatory response to umbilical cord occlusions with worsening acidosis in the ovine fetus. *Am J Obstet Gynecol* 202, 1 (2010), 82.

[52] RICHARDSON, B., RURAK, D., PATRICK, J., HOMAN, J., AND CARMICHAEL, L. Cerebral oxidative metabolism during sustained hypoxaemia in fetal sheep. *J Dev Physiol* 11, 1 (1989), 37–43.

[53] RICHMAN, J., AND MOORMAN, R. Time series analysis using approximate entropy and sample entropy. *Biophysical Journal* 78, 1 (Jan. 2000), 218A–218A.

[54] RICHMAN, J. S., AND MOORMAN, J. R. Physiological time-series analysis using approximate entropy and sample entropy. *Am J Physiol Heart Circ Physiol* 278, 6 (Jun 2000), H2039–H2049.

[55] SHANNON, C. A mathematical theory of communication. *The Bell System Technical Journal* 27 (1948), 388–427.

[56] SIIRA, S., OJALA, T. H., VAHLBERG, T. J., ROSÉN, K. G., AND EKHOLM, E. M. Do spectral bands of fetal heart rate variability associate with concomitant fetal scalp pH? *Early Hum Dev* 89, 9 (Sep 2013), 739–742.

[57] SIIRA, S. M., ET AL. Marked fetal acidosis and specific changes in power spectrum analysis of fetal heart rate variability recorded during the last hour of labour. *BJOG* 112, 4 (Apr 2005), 418–423.

[58] SPILKA, J., CHUDÁČEK, V., KOUCKÝ, M., LHOTSKÁ, L., HUPTYCH, M., JANKŮ, P., GEORGULAS, G., AND STYLIOS, C. Using nonlinear features for fetal heart rate classification. *Biomedical Signal Processing and Control* 7, 4 (2012), 350–357.

[59] SPILKA, J., FRECON, J., LEONARDUZZI, R., PUSTELNIK, N., ABRY, P., AND DORET, M. Sparse support vector machine for intrapartum fetal heart rate classification. *IEEE Journal of Biomedical and Health Informatics PP* (2016), 1–1.

[60] SPILKA, J., FRECON, J., LEONARDUZZI, R., PUSTELNIK, N., ABRY, P., AND DORET, M. Sparse support vector machine for intrapartum fetal heart rate classification. *IEEE J Biomed and Health Inform* 21 (2017), 664–671.

[61] SPILKA, J., ROUX, S., GARNIER, N., ABRY, P., GONCALVES, P., AND DORET, M. Nearest-neighbor based wavelet entropy rate measures for intrapartum fetal heart rate variability. In *Engineering in Medicine and Biology Society (EMBC), 2014 36th Annual International Conference of the IEEE* (Aug 2014), pp. 2813–2816.

[62] SPILKA, J., ROUX, S., GARNIER, N., ABRY, P., GONCALVES, P., AND DORET, M. Nearest-neighbor based wavelet entropy rate measures for intrapartum fetal heart rate variability. *Conf. Proc. of the IEEE Eng. Med. Biol. Soc. (EMBC)* (2014), 2813–2816.

[63] VAN LAAR, J., PORATH, M., PETERS, C., AND OEI, S. Spectral analysis of fetal heart rate variability for fetal surveillance: Review of the literature. *Acta Obstet. Gynecol. Scand.* 87, 3 (2008), 300–306.

[64] WARRICK, P., HAMILTON, E., PRECUP, D., AND KEARNEY, R. Classification of normal and hypoxic fetuses from systems modeling of intrapartum cardiotocography. *IEEE Transactions on Biomedical Engineering* 57, 4 (2010), 771–779.

[65] XU, L., REDMAN, C. W., PAYNE, S. J., AND GEORGIEVA, A. Feature selection using genetic algorithms for fetal heart rate analysis. *Physiol meas* 35, 7 (2014), 1357–71.

	animal (ID)	CVD time t_{CVD} (hh:mm:ss)	D time t_D (hh:mm:ss)	delta $t_{\text{CVD}} - t_D$ (hh:mm:ss)
Hypoxic	8003	03:09:07	03:10:10	-00:00:53
	473351	05:19:01	05:19:19	-00:00:58
	473362	03:07:04	03:24:24	-00:17:45
	473376	04:42:44	04:59:59	-00:17:15
	473726	04:09:56	04:04:04	00:04:56
Normoxic		06:29:29	05:02:12	00:12:26
		473361	05:04:42	00:19:56
		473352	05:08:02	00:03:01
		473377	04:42:09	-00:07:35
		473378	05:23:40	00:08:40
		473727	03:12:27	-00:17:32
		5054	04:56:16	-00:03:28
		5060	03:43:56	00:14:07
		473360	05:51:46	02:56:54

Table 4: Cardiovascular decompensation (CVD) times. Comparison of the visually determined versus computed predictions: t_{ABP} from [33] as reference, and our new distance time t_D , computed by requiring $D > 2.5$ for at least 3 consecutive time-windows, spanning a total duration of 30 minutes. The last column reports the difference $t_{\text{ABP}} - t_D$ between the reference ABP time, always earlier than t_{pH} , and the new t_D . Positive values indicate a detection earlier than the ABP sentinel. All data are derived from 4 Hz sampled FHR signal.